An effective QWBA/UHPLC-MS/tissue punch approach: solving a pharmacokinetic issue via quantitative Met-ID

József Pánczél*[1], Manfred Schudok[1], Matthias Schiell[1], Jens Riedel[1], Vilmos Kertesz[2]

[1]Research and Development, DMPK, Sanofi-Aventis Deutschland GmbH, Frankfurt, Germany

[2]Bioanalytical Mass Spectrometry Group, Biological Sciences Division, Oak Ridge National Laboratory, Oak Ridge, TN 37831, USA

*Corresponding Author

Submitted to **Drug Metabolism Letters**

Address reprint requests to:

József Pánczél

Drug Metabolism and Pharmacokinetics, Metabolism

Industriepark Hoechst, G876, 65926 Frankfurt am Main, Germany

Email: Jozsef.Panczel@sanofi.com

Background: Methods to provide absolute quantitation of the administered drug and corresponding metabolites in tissue in a spatially resolved manner is a challenging but much needed necessity in pharmaceutical research. Quantitative whole-body autoradiography (QWBA) after a single-dose intravenous (3 mg/kg) and extravascular (30 mg/kg) administrations of an *in vitro* metabolically stable test compound (structure not reported here) indicated quick tissue distribution and excretion.

Objective: Good bioavailability and short *in vivo* half-lives were determined formerly for the same test compound. For closing gaps in the understanding of pharmacokinetic data and *in vitro* results, radioactive hot spots on whole-body tissue sections had been profiled.

Method: Punches from selected tissue regions containing high radioactivity in the tissue sections previously analyzed by QWBA were extracted by a highly organic solvent and analyzed without any consecutive sample preparation step, applying ultra high performance liquid chromatography-mass spectrometry (UHPLC-MS) and off-line radioanalysis to maximize signal levels for metabolite identification and profiling.

Results: The analysis revealed that the test compound was metabolized intensively by phase I reactions *in vivo* and the metabolites formed were excreted in bile and in urine. The predominant metabolites showed abundant signal intensities both by MS and by radioanalysis but the MS signal intensities generally underestimated the real abundances of metabolites relative to the unchanged drug.

Conclusions: This work illustrates that maximizing the sensitivity of tissue punch radioanalysis and the combination with UHPLC-MS leads to a better insight of pharmacokinetic processes by providing quantitative data with high molecular selectivity.

Keywords: QWBA, UHPLC-MS, radioanalysis, tissue punch, absolute quantitation, metabolite

TOC

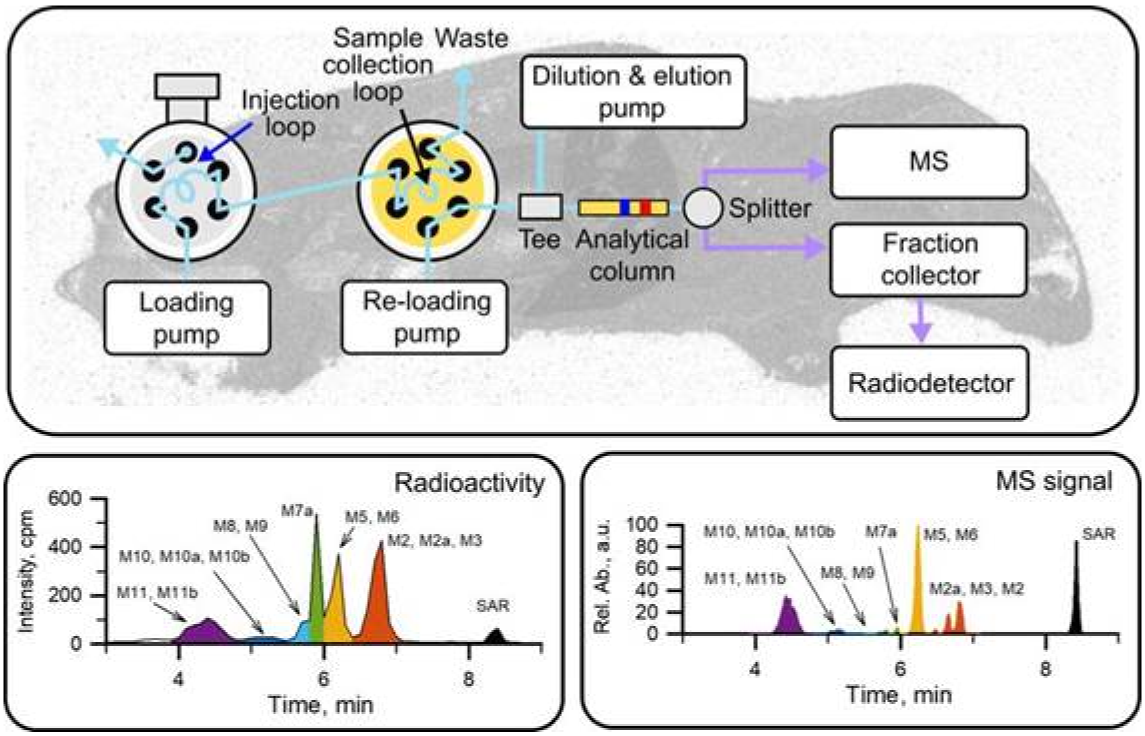

1 INTRODUCTION

Spatially resolved quantitative determination of drugs and their metabolites in tissues is important in pharmaceutical research where such information is used to predict pharmacological target engagement, toxicological target tissue exposure, and drug disposition, among other purposes [1]. Quantitative whole-body autoradiography (QWBA) is most often used to quantitatively resolve drug concentrations with sub-100 µm spatial resolution [2, 3, 4, 5]. Unfortunately, the technique cannot differentiate between a drug and its associated metabolites that hinders its applicability for their simultaneous profiling. For that reason, spatially resolved quantitative molecular characterization of tissue can be better accomplished by tissue punch/liquid chromatography-mass spectrometry (LC-MS). In this method, a small tissue section is physically cut from the surrounding tissue using commercially available tissue biopsy punches. The isolated tissue section can then be processed and chemically characterized by LC-MS with about 1-3 mm spatial resolution [6]. LC-MS can provide high chemical specificity enabling simultaneous measure of the drug, its associated metabolites and even endogenous molecules. However, like any other tissue profiling methods employing MS investigated for quantitative capabilities (notably matrix-assisted laser desorption/ionization MS imaging [7, 8, 9, 10, 11, 12], desorption electrospray ionization [13, 14], nanospray desorption electrospray ionization MS [15, 16], liquid extraction surface analysis [17, 18], exhaustive liquid microjunction surface sampling [19], and the dropletProbe system [20]), it requires all appropriate internal standards to be employed, if quantitation is required.

Previously, the combination of QWBA and consecutive separation of radioactive drug and metabolites extracted by tissue punches were demonstrated using thin layer chromatography [21] and high performance LC (HPLC) [22]. However, in these and similar studies only a fraction of the extracted analytes were utilized/injected on the separation column. This fact along with the already low initial concentration of the parent drug hindered sensitivity.

In this paper, QWBA analysis of whole-body mouse slices and corresponding ultrahigh performance liquid chromatography [23, 24, 25, 26, 27, 28, 29, 30, 31, 32, 33] (UHPLC)-MS analysis of 3-mm-diameter tissue punches with known total radioactivity (drug and metabolites) are presented, with complete extraction of drug-related compounds been utilized in the latter analysis. The goal of this study was to investigate the distribution, possible accumulation and excretion of the test compound (shortened here as SAR) in mouse. The *in vitro* metabolism of SAR (structure not reported here) showed a low biotransformation rate. Good bioavailability, short half-lives [34] and low amounts of excreted unchanged drug were observed in pharmacokinetic studies performed for SAR in mouse. The radioactivity hot spots assessed by QWBA had to be analyzed, especially in the gastrointestinal and urinary tracts, to reveal the *in vivo* fate of SAR in mouse and to find the root cause of inconsistencies in the pharmacokinetic results.

2 MATERIALS AND METHODS

2.1 Materials

Optima™ LC/MS grade water, acetonitrile (ACN), formic acid (FA) and trifluoroacetic acid (TFA) were purchased from Thermo Fisher Scientific (Waltham, MA, USA).

2.2 Tissue preparation

Animal experiments were performed according to internal guidelines and governmental requirements. Thin tissue sections were prepared from male C57BL/6J mice (approximately 25 – 30 g each, Charles River Laboratories, Sulzfeld, Germany) administered a single intravenous dose of 3 mg/kg or a single oral dose of 30 mg/kg of 14C-labeled SAR, corresponding to a radioactive dose of 2.2923 MBq/kg for the intravenous (IV)-arm of the study and 7.065 MBq/kg for the per oral (PO)-arm. At 0.1h (IV administration) or 1h, 4h and 8h (PO administration) postdose mice were euthanized with an isoflurane overdose and immediately frozen in dry ice/hexane at -70 °C. Limbs and tail of the animals were removed, followed by wrapping the carcasses in paper towel and placed them in a plastic bag at -20 °C overnight for equilibration followed by embedding in carboxymethylcellulose (Metylan, Henkel, Düsseldorf) with the left lateral side uppermost. Sagittal whole-body cryosections (40-µm-thick) were prepared using a cryomicrotome (Leica CM3600, Leica Microsystems, Wetzlar, Germany). Serial sections of 40 µm thickness were collected onto 8210 Scotch® tape (3M, St. Paul, MN), then the sections were freeze-dried within the chamber of the cryomicrotome.

2.3 QWBA analysis

After freeze-drying for 24 h, sections were exposed on Fuji imaging plates for 24 h at room temperature and analyzed with a FujiFilm BAS5000 Bio-imaging Analyzer (Fuji Film Co. Ltd., Tokyo, Japan). Organs and tissues for detailed evaluation were selected after visual inspection of the exposed radioluminograms. Analysis of the samples was done by using AIDA software (Elysia-raytest GmbH, Straubenhardt, Germany): For the marked areas in the radioluminograms the concentration of radioactivity was expressed as PSL (photon stimulated luminescence)/mm^2 and converted to ngEq/g tissue by using a blood calibration curve. To determine lowest limit of quantitation (LLOQ), five background areas were determined on each imaging plate; mean background plus three times the standard deviation is defined as the LLOQ. The mean LLOQ value for each time point was calculated from the individual LLOQ values determined for each slice of the same time point. The upper limit of quantitation (ULOQ) is per definition the maximum of the dynamic range of the imaging plates, 3500 PSL/mm^2.

2.4 Tissue punch extraction

Tissue punches – to be sampled based on the radioactivity – with a diameter of 3 mm were created from the whole-body tissue sections by a core sampling tool (Electron Microscopy Sciences, Hatfield, PA, USA) and placed into low-bind 1.5 ml Eppendorf tubes containing 100 µL of 75:25 ACN:water with 0.1% TFA extraction solvent (Figure 1a). The vial was vortexed (model Eppendorf Thermomixer Comfort, Brinkmann Instruments, Inc., Westbury, NY, USA) for 15 minutes at 1000 rpm (Figure 1b) followed by centrifuging (model Eppendorf Centrifuge 5417 R, Brinkmann Instruments, Inc., Westbury, NY, USA) for 15 minutes at 14000 rpm at 4 ^{o}C (Figure 1c) then the sample was diluted by 150 µL water with 0.1% TFA. After centrifugation the entire supernatant was transferred into a TrueView^{TM} LC-MS certified sample vial (Waters, Milford, MA, USA) (Figure 1d).

2.5 UHPLC-MS analysis

The multidimensional UHPLC system consisted of Agilent 1100 (Agilent Technologies, Santa Clara, CA, USA) and UltiMate 3000 modules Thermo Fisher Scientific, Waltham, MA, USA). After a tissue punch was extracted according to the protocol described above, 200 µL sample was subjected to UHPLC-MS analysis and off-line radioanalysis. The following injection technique allowed the injection of the entire 200 µL sample with relatively high organic content – 30% acetonitrile – onto a C-18 RP-HPLC column: the sample was injected into the injection loop of an Agilent 1100 autosampler (Figure 1e) and transferred into the sample collection loop with a capacity of 1000 µL by an Agilent 1100 “loading” pump (Figure 1f). From there an UltiMate 3000 “reloading” pump loaded the sample onto the analytical column (XSelect HSS T3 2.5 µm, 3.0 mm x 100 mm; Waters, Milford, MA, USA) equipped with its guard column (same stationary phase) held constantly at 40 °C while another UltiMate 3000 “dilution and elution” pump diluted the loading flow using a tee in a ratio of 1 to 10 (Figure 1g). Both the “re-loading” and the “dilution and elution” pumps pumped 0.1% TFA in water (0.175 mL/min and 1.575 mL/min, respectively). This dilution ensured 3% or lower organic content of sample flow (some dilution of sample occurred already in the transfer steps) in the loading to the analytical column, ensured efficient trapping of analytes at the front of the analytical column enhanced further by the ion pair formation effect of TFA. The UHPLC separation utilized two mobile phases consisting of 0.1 % formic acid in water (eluent A) and 0.1 % formic acid in ACN (eluent B) to wash TFA from the UHPLC column as well as to avoid any decrease in the MS signal intensities. The linear eluent gradient (1 ml/min, 0 % to 97 % eluent B in 23 min) was provided by the "dilution and elution" pump. Finally, the eluate was split for simultaneous MS analysis (1/4 part of eluate) and fraction collection (3/4 part of eluate) for off-line radioanalysis

The MS analyses were run on a Fusion ETD (Thermo Fisher Scientific, Waltham, MA, USA) mass spectrometer equipped with a H-ESI ion source that operated in positive mode (+3500 V). The Ion Transfer Tube and Vaporizer temperatures were set to 325 °C and 350 °C, respectively. Sheath gas, auxiliary gas, sweep gas were utilized to 50, 10 and 0 gas flows (arbitrary units all), respectively. Mass spectra were recorded in full scan (resolution: FWHM 120.000 @ m/z 200) and in dd-MS2 and dd-MS3 modes (resolution: FWHM 60.000 @ m/z 200 for both) with HCD and CID fragmentations.

2.6 Off-line radioanalysis

The UHPLC eluent was fractionated (Gilson FC 204 fraction collector; Gilson, Middleton, WI, USA) by collecting approximately 75 μL fractions into 96-well Lumaplates (PerkinElmer, Waltham, MA, USA) at every 6 seconds. Each well was analyzed by TopCount (PerkinElmer, Waltham, MA, USA) radioscintillation plate reader for 5 min.

2.7 Data evaluation

Metabolite identification was performed using Mass-Metasite software package version 3.4.1 (Molecular Discovery, Borehamwood, UK) and the single sample evaluations were uploaded and clustered in WebMetabase 4.0.6 (Molecular Discovery, UK). Phase I and phase II reactions were allowed with 3 consecutive metabolic steps including unexpected products, multiple charged ions up to charge state of 2, neutral losses and dimeric ions. The computed peaks were rescued and split in order to obtain all possible metabolites. The raw data files created by TopCount were evaluated by the software package Laura version 4.2. (LabLogic, Sheffield, UK).

3 RESULTS AND DISCUSSION

3.1 General pharmacokinetic findings of SAR

The radioactivity derived from SAR was quickly and widely distributed both after IV and PO administration (see Supplementary Table S1). After both type of administrations highest radioactivity levels were found in bile, urinary bladder, liver and stomach/intestines, already after the short timeframe of 0.1 h in case of IV administration. These observations indicated quick excretion of SAR.

SAR was found metabolically stable in prior *in vitro* liver microsomal and cryopreserved hepatocyte incubations of human, mouse and rat (see Supplementary Summary S10). SAR showed 89% bioavailability in parallel with short terminal half-lives in blood (0.59 h and 0.68 h after IV and PO administration, respectively, see Supplementary Summary S11).

3.2 Metabolite identification and metabolic profiling by UHPLC-MS of tissue regions

All tissue regions reported in this paper were analyzed by UHPLC-MS and the metabolic identification was performed in each sample by Mass-Metasite then the identified metabolites were clustered in WebMetabase. Figure 2 shows the identified metabolic pathways and metabolites of SAR (metabolite structures are not reported here). The same volumes of tissue samples (a diameter of 3 mm with 40 μm thickness) were punched out for all tissues and at all sampling times to compare the metabolic profiles over the tissues and sampling time properly. The UHPLC-MS peak area-based metabolic profiles were compared among the different tissues at each sampling time then within the same tissue over the sampling time as shown in Figures 3-6. Finally, the LC-MS based metabolic profiles were compared to some simultaneously recorded radioanalytical profiles as shown in Figure 7 to assess the possible differences in MS ionisation of different metabolites. The findings for the different organs are concluded below.

Stomach

Mainly unchanged drug was observed up to 4h after PO administration in stomach samples (see Supplementary Tables S2 and S3). The observed metabolic profile in the 8h sample after PO administration suggested that some degradation of SAR occurred in stomach.

Liver and kidney

In liver and kidney samples (see Supplementary Tables S4 and S5) high intensities of unchanged drug and low relative abundances of metabolites were observed up to 4h. In the 8h sample metabolites M2, M5 and M11 showed higher relative abundances with a decrease of 2 to 3 orders of magnitude in sum of all UHPLC-MS peak areas compared to 1h sample.

Urinary bladder

In urinary bladder samples high intensities of drug related materials were observed for all time points up to 8h indicating quick excretion. In the early time point of 0.1h after IV administration (see Supplementary Tables S2 and S6) the metabolites were less abundant relative to unchanged drug. The increase of relative abundances of metabolites was observed by the time in the other samples. The main metabolic pathways were the ring opening by N-dealkylation (M2), further oxidations of M2 to M5, M10b, M11 or glucuronidation of – most possibly M2 – to M7a. Abundant hydroxyl (M3, M6) and hydroxy-glucuronide metabolites (M8, M9) were observed in urinary bladder in 4h and 8h as well.

Bile (gallbladder)

In bile samples high intensities of drug related materials were observed up to 8h (see Supplementary Table S7). The high amount of SAR in 0.1h bile sample after IV administration indicated quick excretion into bile as well. The relative abundances of metabolites to unchanged drug were low both in samples of 0.1h after IV administration and in 1h after PO administration. The metabolites M2, M5 and M11 were dominating in the metabolic profile in 8h sample after PO administration and higher amount of glucuronide conjugates (M4, M7a, M8, M9) were observed. The metabolite profiles observed in bile and in liver at 8h differed in metabolic profiles significantly indicating excretion of metabolites from liver into bile.

Large intestines

In large intestines unchanged drug was identified mainly in early time points up to 1h (see Supplementary Table S8). Comparing the intestine metabolic profile to that of bile similar trends were observed at 8h for the main oxidative metabolic pathways (M2 with its further oxidated and hydroxylated metabolites). The glucuronide metabolites were observed in large intestines in the 4h sample only.

Rectum

In rectum samples an increase in the amount of drug related metabolites was observed as postdose time increased. Similar profiles were observed between the 8h rectum profile, and the 4h and 8h large intestine profiles (see Supplementary Tables S2 and S9).

3.3 Comparison of the metabolic profiles determined by UHPLC-MS and radiochromatography

The injection of the whole tissue punch extract was crucial to generate radioprofiles of tissue regions where the radioactivity was high enough to try to perform such an experiment at all. This simultaneous radioprofiling was important to assess the real abundances of metabolites and to correct the differences in mass spectrometric ionisation efficiencies of different metabolites in the comparison to the LC-MS based profiles. Figure 7 shows the metabolites of SAR were underestimated by LC-MS profiling. As an example, the UHPLC-MS peak areas of M11 and M11b represented 121% and 8.8% of the unchanged drug peak area (see Supplementary Tables S2 and S6), respectively but M11 and M11b represented 16% of total radioactivity while the unchanged drug 4% only. By comparing the UHPLC-MS and radioactivity peak abundances the predominant metabolites were abundant in the UHPLC-MS profiles – except for M7a – as well just usually underestimated with a factor of 3 – 5. The difference was especially high for M7a (glucuronide of M2) only: M7a was ionized approximately two orders of magnitude weaker than the unchanged drug. M7a was a consecutive metabolite of M2 and so belonged to the most important pathway of SAR as well.

As a consequence both the LC-MS based and radioanalytical profiling confirmed the main metabolic pathways of SAR discussed in the next chapter.

3.4 The fate of SAR in mouse *in vivo*

Figures 3-6 show the abundances of drug related materials as the function of sampling time and organs as relative extracted ion abundances of parent drug and each metabolite or metabolite group that belonged to the same biotransformation step as well as the total radioactivity. 100% for a given metabolite or a group of metabolites reflects of the maximum signal measured for all organs and time points.

QWBA results indicated quick distribution and excretion of drug related materials already at 0.1h after IV administration. Comparable concentrations of drug related materials were determined in liver, kidney, gallbladder and in urinary bladder and the unchanged drug was predominant in these tissues investigated at 0.1h.

The concentrations of drug related materials were comparable in stomach, gallbladder and in urinary bladder at 1h, but not in liver and in kidney due to incomplete drug absorption but with simultaneously occurring quick excretion. SAR represented 13% of total radioactivity in urinary bladder only while the majority of radioactivity derived from M2 and its consecutive metabolites. Regarding the gastrointestinal tract SAR seemed to be predominant in bile and a relatively low amount of drug related materials reached already the regions of large intestines that consisted of unchanged drug mainly, similarly to bile at 1h.

The drug related materials were depleted already from stomach at 4h. They reached the large intestines and they were further excreted in urinary bladder. They mainly consisted of M2 and consecutive metabolites. The metabolites did not get to rectum according to its metabolite profile showing lower abundances of metabolites in rectum relative to SAR. No accumulation of radioactivity was observed in any organ and at all time points, and no metabolite was identified without radiolabel. Unfortunately, gallbladder was not identified on any tissue section at 4h but it surely contained a presumably high amount of drug related materials as it was a radioactivity soft spot both at 1h and 8h.

The concentration of drug related materials decreased in urine for 8h compared to 4h while the relative abundances of M2 and its consecutive metabolites further increased in urine. This trend was found for liver and kidney as well, and a shift of all drug related materials was observed to rectum in the gastrointestinal tract with a further increase in the relative abundances of M2 and its related metabolites. SAR represented already a minor fraction only both in gastrointestinal and urinary tracts at 8h. The excretion of metabolites occurred already into bile and urine at 8h. However, it was a quicker process in kidney compared to liver since very high radioactivity concentration was determined in large intestines at 8h which was comparable with bile.

As a summary, the *in vitro* very stable SAR was metabolized *in vivo* extensively by the in vitro already identified biotransformation steps, and its metabolites were excreted in urine and in bile. Up to 8h high amounts of excreted drug related materials were determined in urinary bladder and from bile to rectum. Simultaneously, a decrease in the relative amount of unchanged drug was observed as postdose time increased. The main *in vivo* metabolic pathways – similarly to in vitro – were the ring opening by N-dealkylation (M2), oxidation of M2 to carboxyl (M5), further O-dealkylation of M2 to M11, hydroxylation of M2 to M9a and M10b, and glucuronidation of M2 to M7a. The following pathways were determined with subordinate abundances: N- or O-dealkylation (M10, M11b), hydroxylations (M3, M6, M11a) and hydroxy-glucuronidations (M4, M8, M9).

The higher relative abundances of glucuronide metabolites (M4, M7a, M8, M9) were decreased in large intestines and in rectum compared to bile suggesting their cleavage by glucuronidase enzymes. The relatively higher abundances of M3, M6, M2, and M5 metabolites implies the support this reaction or further oxidation in intestinal tract. Regarding M5 and M11 – further oxidation products of M2 – their signal in the 8h rectum profile was between the 4h and 8h large intestine profiles, and the 8h bile profile contained slightly less relative amount of M5 and M11 compared to the 8h large intestine profile.

CONCLUSION

Here we reported the elucidation of the root cause of short *in vivo* half-lives in contrast to prior *in vitro* results. The injection of entire extracts from QWBA thin tissue punches provided chromatographic signal intensities comparable to conventional UHPLC analysis. QWBA results indicated quick distribution and excretion of drug related materials of the *in vitro* metabolically stable SAR. The metabolite identification and profiling in the extracts of gastrointestinal and urinary tracts revealed the intensive metabolism of SAR and excretion of drug related materials into bile and urine.

The advancement presented here allowed simultaneously metabolite profiling of radioactivity hot spots on whole-body tissue sections identified by QWBA, not only by UHPLC-MS but radioscintillation as well, with the additional advantage of structure elucidation of metabolites. This approach widely applicable in case of QWBA results (showing the total radioactivity distribution), to extend the knowledge towards quantitative drug and metabolite characterization from available slices. Regarding future studies we recommend an appropriate dose of radioactivity and sampling of the tissue regions at properly selected tissue levels. This is crucial for a targeted metabolite profiling of the tissues of interest.

ACKNOWLEDGEMENTS

The work of V.K. was supported by the U.S. Department of Energy, Office of Science, Biological and Environmental Research, Bioimaging Science Program.

ORCID

József Pánczél	https://orcid.org/0000-0002-8188-5714
Manfred Schudok	https://orcid.org/0000-0001-6372-5672
Matthias Schiell	https://orcid.org/0000-0002-4595-3118
Jens Riedel	https://orcid.org/0000-0002-6801-5212
Vilmos Kertesz	https://orcid.org/0000-0003-0186-5797

.

FIGURE CAPTIONS

Figure 1. Schematic of the tissue punch protocol including (a) punching out the tissue samples, (b) vortexing the sample in the extraction solvent, (c) centrifuging the extract to separate solid phases and supernatant, (d) drawing the supernatant into the autosampler syringe and (e) loading into the injection loop followed by (f) injection into a sample collection loop, and (g) diluting onto an analytical column for a consecutive HPLC-MS analysis and fraction collection for offline radioanalysis.

Figure 2. Identified metabolic pathways of SAR.

Figure 3. Distribution of radioactivity, parent and metabolites drug mass spectrometry signal in the gastrointestinal tract over time. Calculated relative extracted ion abundances of parent drug (black line), sum of M4+M8+M9 (purple line), sum of M3+M6+M11a (blue line), M2 (light blue line), M5 (green line), M7a (orange line), sum of M9a+M10b (red line), M11 (dark red line) and the sum of M10+M11b (black dashed line), as well as total radioactivity (dashed dark red line) as a function of the analyzed organ measured at (a) 0.1h, (b) 1h, (c) 4h and (d) 8h post dose. 100% for a given metabolite or a group of metabolites reflects of the maximum signal measured for all organs and time points. Triple asterisks (***) indicate interpolated data calculated from timepoints measured before and after for the specific organ. Radioactivity was not measured for rectum.

Figure 4. Distribution of radioactivity, parent and metabolites drug mass spectrometry signal in individual organs of gastrointestinal tract as a function of time. Calculated relative

extracted ion abundances of parent drug (black line), sum of M4+M8+M9 (purple line), sum of M3+M6+M11a (blue line), M2 (light blue line), M5 (green line), M7a (orange line), sum of M9a+M10b (red line), M11 (dark red line) and the sum of M10+M11b (black dashed line), as well as total radioactivity (dashed dark red line) as a function of post dose time for (a) stomach, (b) liver, (c) bile, (d) large intestines and (e) rectum. 100% for a given metabolite or a group of metabolites reflects of the maximum signal measured for all organs and time points. Triple asterisks (***) indicate interpolated data calculated from timepoints measured before and after for the specific organ. Radioactivity was not measured for rectum.

Figure 5. Distribution of radioactivity, parent and metabolites drug mass spectrometry signal in stomach, liver and in urinary tract over time. Calculated relative extracted ion abundances of parent drug (black line), sum of M4+M8+M9 (purple line), sum of M3+M6+M11a (blue line), M2 (light blue line), M5 (green line), M7a (orange line), sum of M9a+M10b (red line), M11 (dark red line) and the sum of M10+M11b (black dashed line), as well as total radioactivity (dashed dark red line) as a function of the analyzed organ measured at (a) 0.1h, (b) 1h, (c) 4h and (d) 8h post dose. 100% for a given metabolite or a group of metabolites reflects of the maximum signal measured for all organs and time points.

Figure 6. Distribution of radioactivity, parent and metabolites drug mass spectrometry signal in stomach, liver and in individual organs of gastrointestinal tract as a function of time. Calculated relative extracted ion abundances of parent drug (black line), sum of M4+M8+M9 (purple line), sum of M3+M6+M11a (blue line), M2 (light blue line), M5 (green line), M7a (orange line), sum of M9a+M10b (red line), M11 (dark red line) and the sum of M10+M11b (black dashed

line), as well as total radioactivity (dashed dark red line) as a function of post dose time for (a) stomach, (b) liver, (c) kidney and (d) urinary bladder. 100% for a given metabolite or a group of metabolites reflects of the maximum signal measured for all organs and time points.

Figure 7. (a) Radioanalysis signal obtained offline for fractions collected at every 6 s simultaneously with HPLC-MS analysis. Extracted ion chromatograms (XICs) of *m/z* values (within an m/z interval of ± 2 ppm) corresponding to (b) the parent drug, and metabolites (c) M4, M8, M9 – hydroxylation and glucuronidation; (d) M3, M6 – hydroxylation; (e) M2, M10, M11b – ring opening by N- or O-dealkylation; (f) M2a, M5, M10a – ring opening by N-dealkylation and oxidation to carboxylic acid or dihydroxylation; (g) M7a, M8a – ring opening by N-dealkylation and glucuronidation; (h) M10b – ring opening by N-dealkylation and hydroxylation; and (i) M11 ring opening by N-dealkylation and consequent O-dealkylation. Areas under peaks in (a) are colored accordingly to XICs in (b)-(i) and often indicates signal from multiple metabolites because of co-elutions.

FIGURES

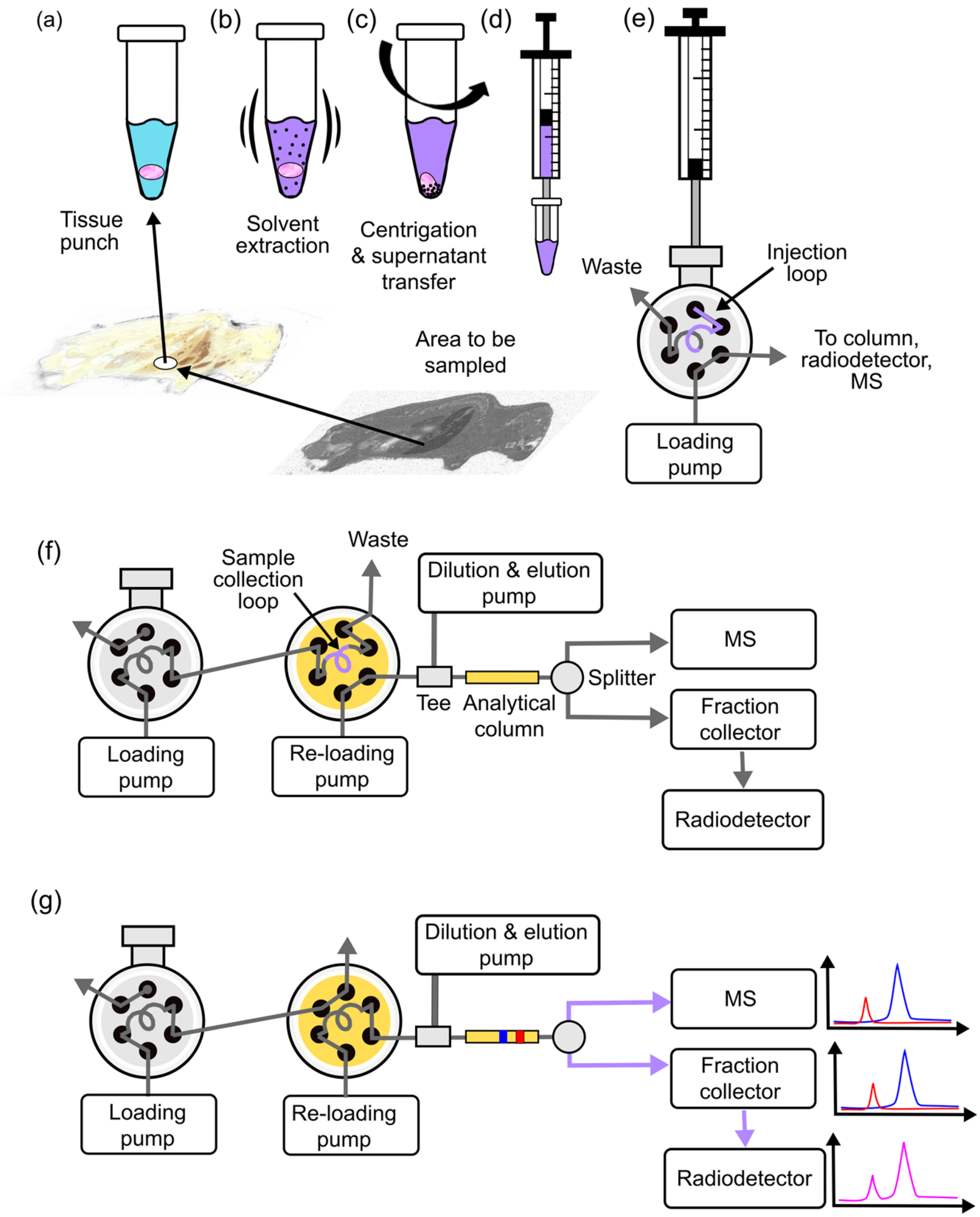

Figure 1.

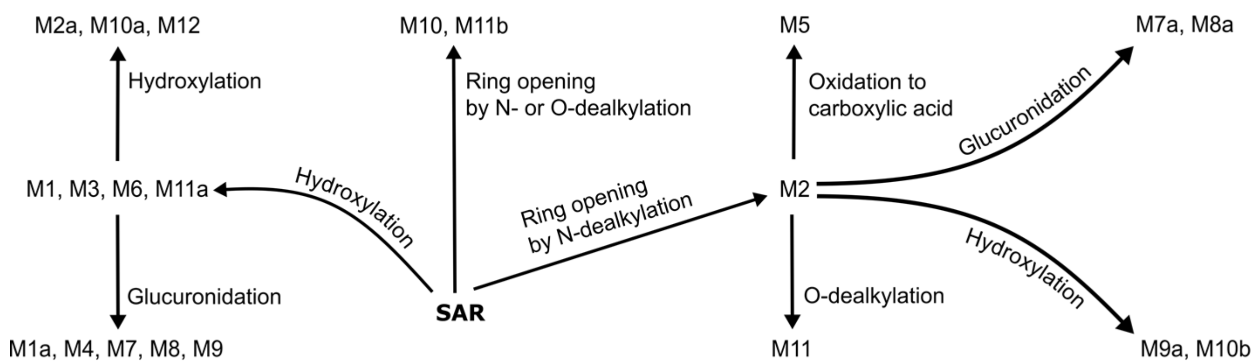

M2a, M10a, M12
Hydroxylation
M1, M3, M6, M11a
Glucuronidation
M1a, M4, M7, M8, M9
Hydroxylation
M10, M11b
Ring opening
by N- or O-dealkylation
SAR
Ring opening
by N-dealkylation
M5
Oxidation to
carboxylic acid
M2
O-dealkylation
M11
Glucuronidation
M7a, M8a
Hydroxylation
M9a, M10b

Figure 2.

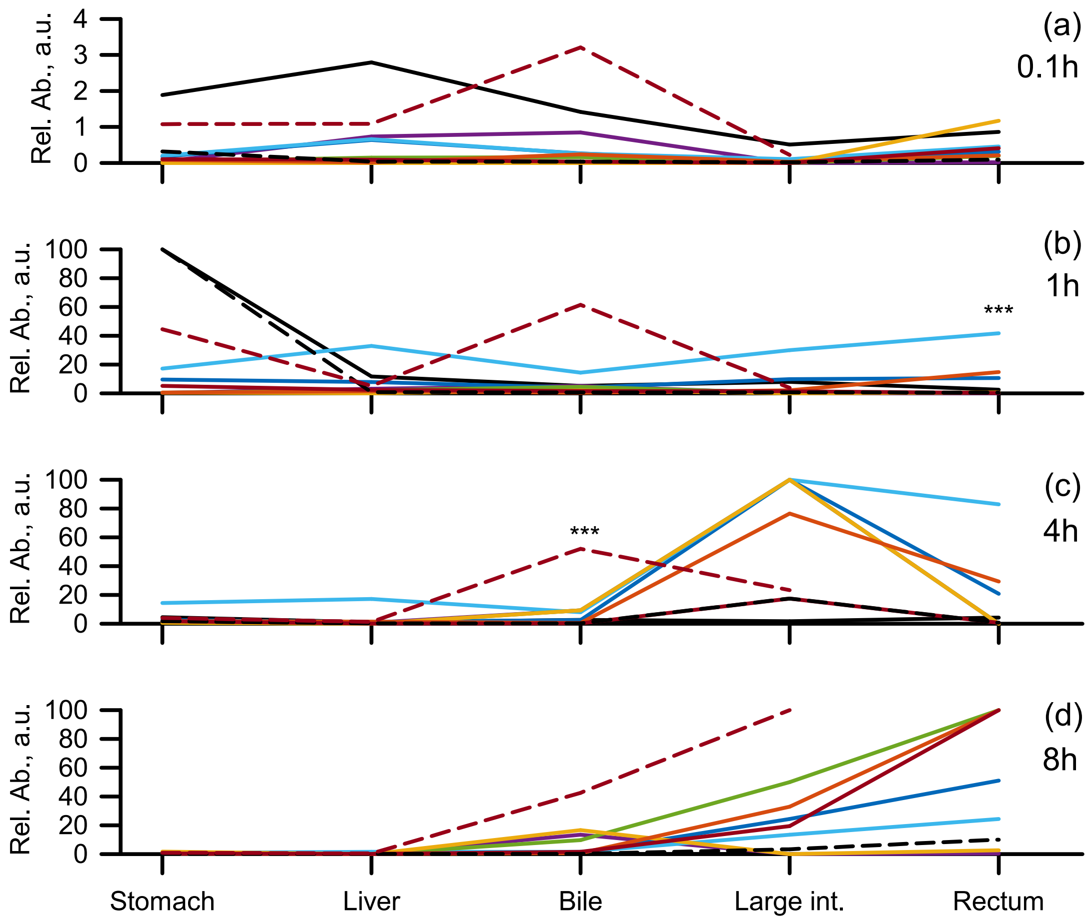

(a)
0.1h
(b)
1h
(c)
4h
(d)
8h
***
***
Rel. Ab., a.u.
0
1
2
3
4
20
40
60
80
100
Stomach
Liver
Bile
Large int.
Rectum

Figure 3.

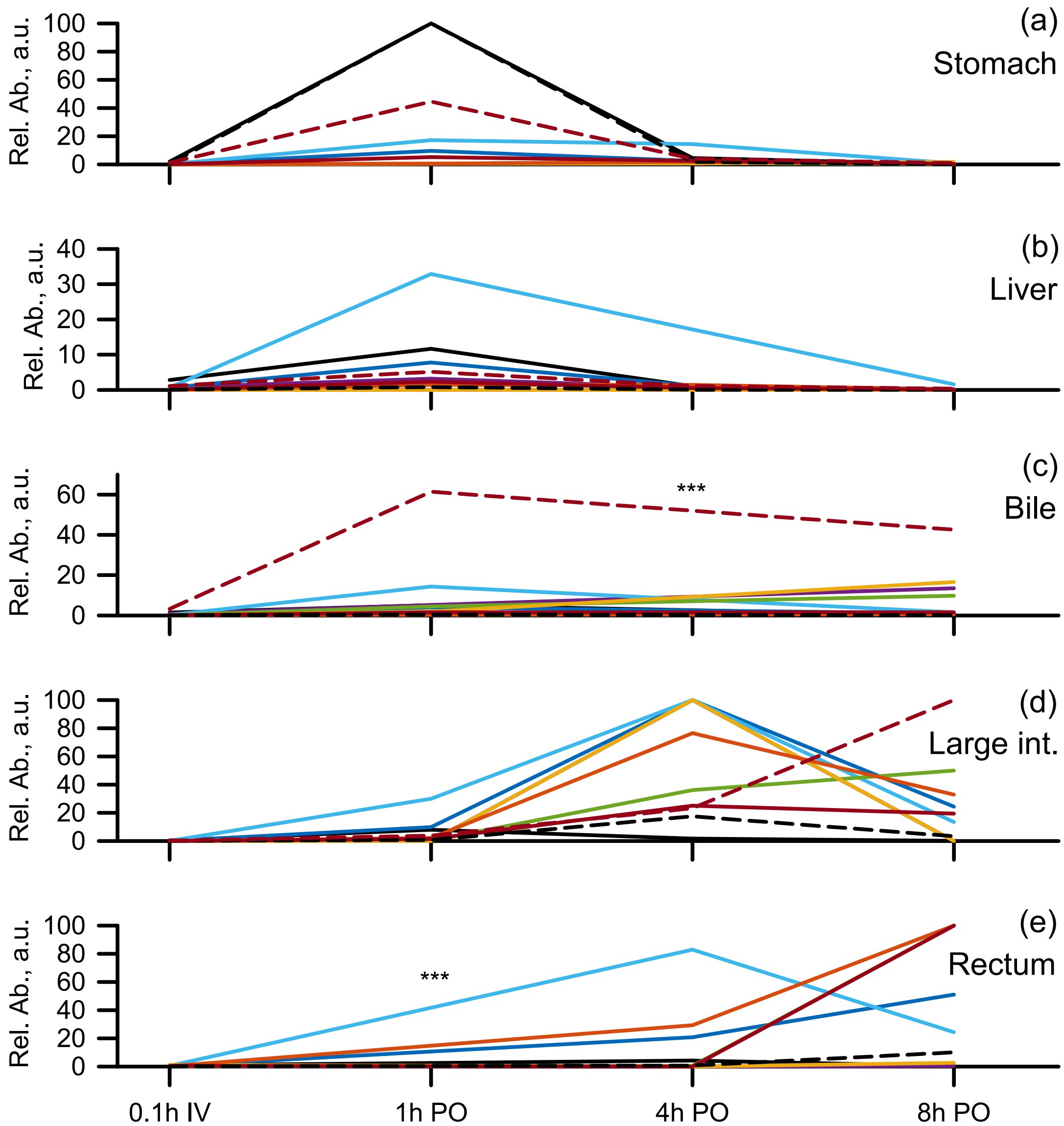

Rel. Ab., a.u.
100
80
60
40
20
0
(a)
Stomach
40
30
20
10
0
(b)
Liver
60
40
20
0
***
(c)
Bile
100
80
60
40
20
0
(d)
Large int.
100
80
60
40
20
0
***
(e)
Rectum
0.1h IV
1h PO
4h PO
8h PO

Figure 4.

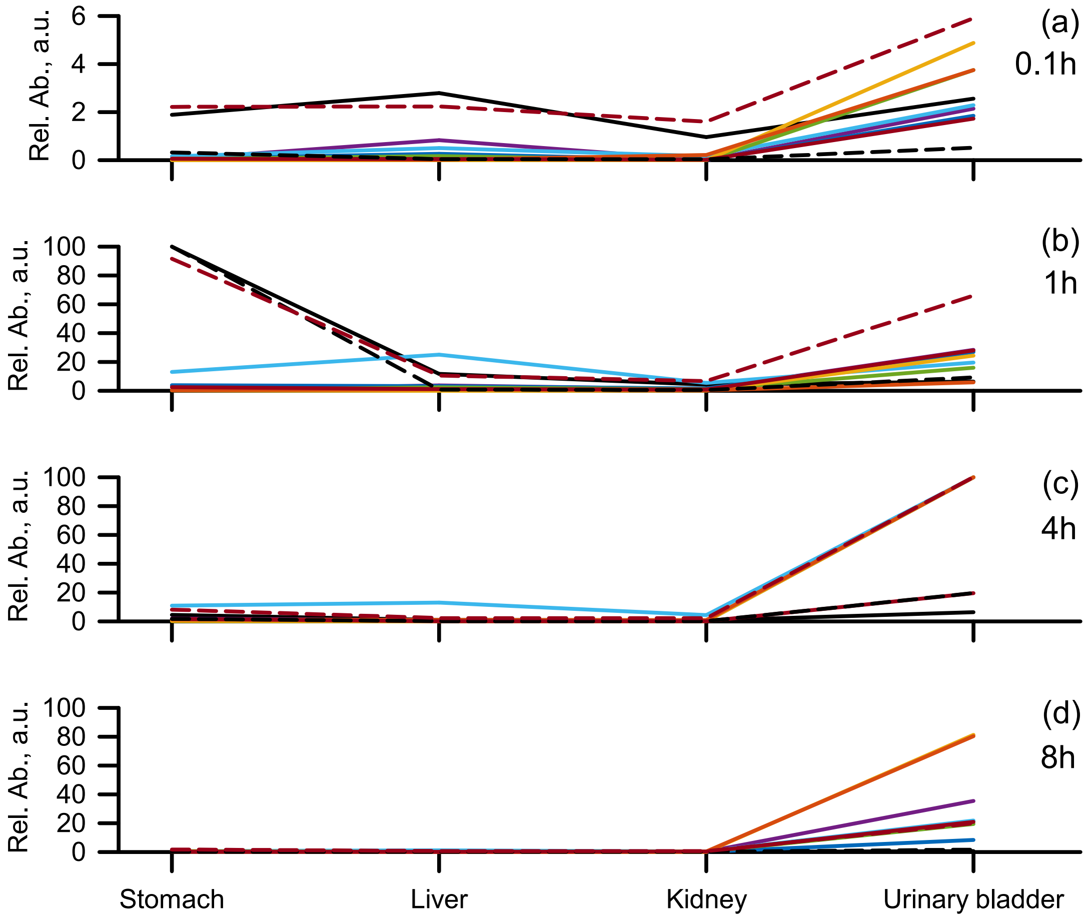

Rel. Ab., a.u.
6
4
2
0
(a)
0.1h
Rel. Ab., a.u.
100
80
60
40
20
0
(b)
1h
Rel. Ab., a.u.
100
80
60
40
20
0
(c)
4h
Rel. Ab., a.u.
100
80
60
40
20
0
(d)
8h
Stomach
Liver
Kidney
Urinary bladder

Figure 5.

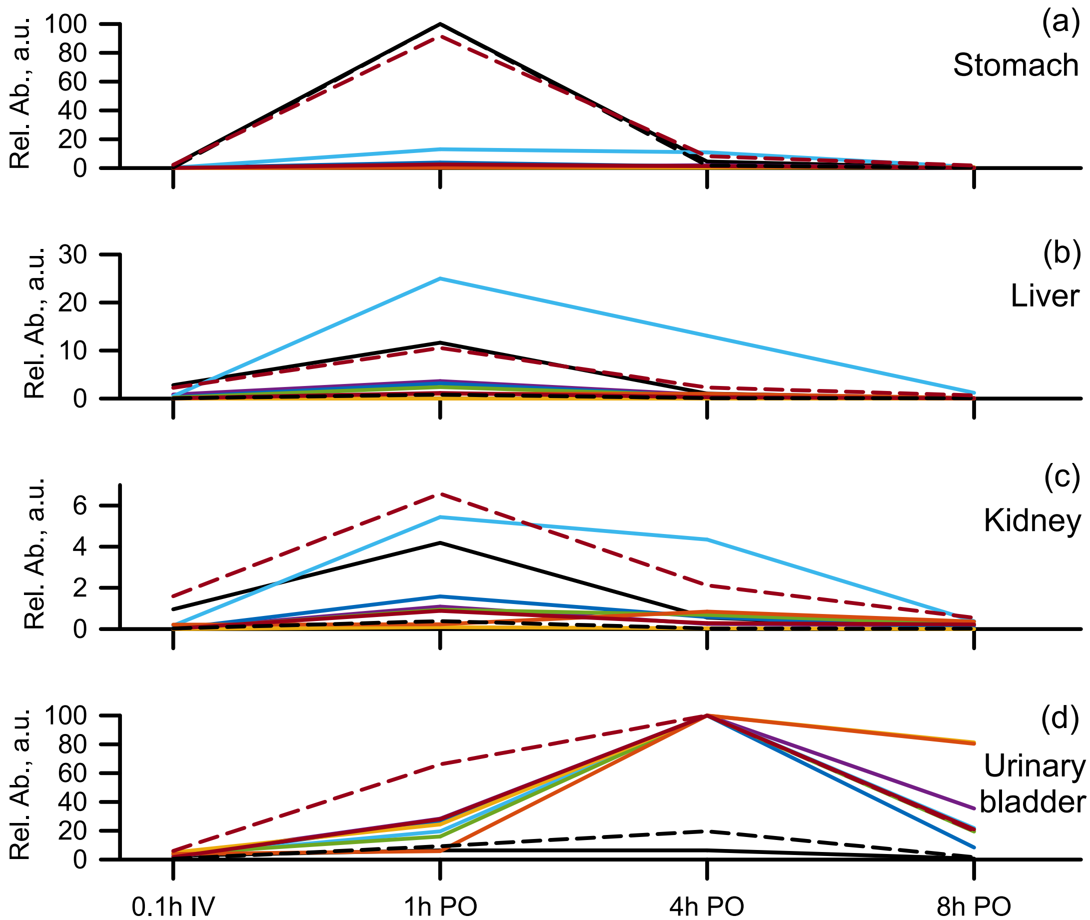

(a)
Stomach
Rel. Ab., a.u.
100
80
60
40
20
0
(b)
Liver
Rel. Ab., a.u.
30
20
10
0
(c)
Kidney
Rel. Ab., a.u.
6
4
2
0
(d)
Urinary bladder
Rel. Ab., a.u.
100
80
60
40
20
0
0.1h IV
1h PO
4h PO
8h PO

Figure 6.

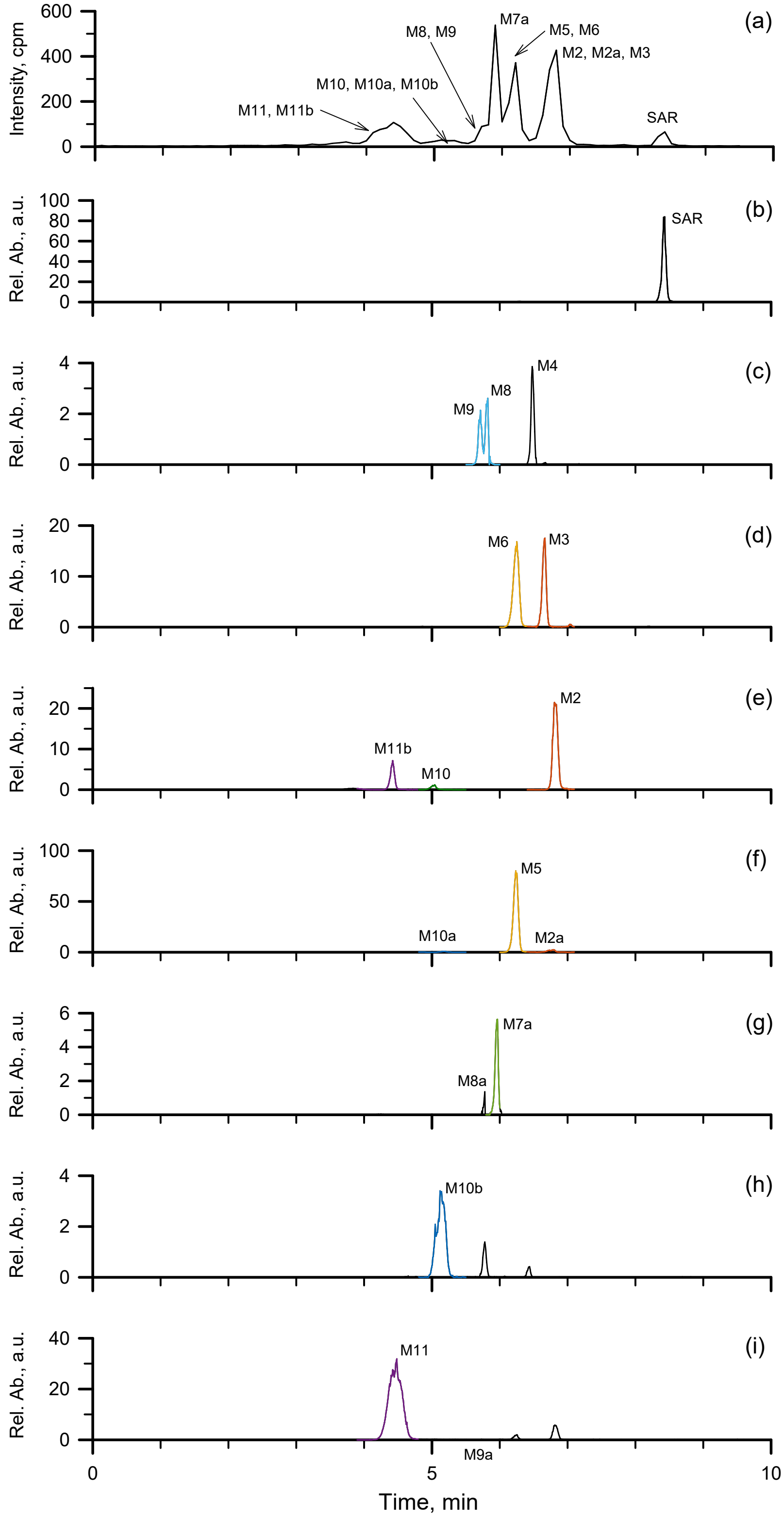

(a)
Intensity, cpm
600
400
200
0
M11, M11b
M10, M10a, M10b
M8, M9
M7a
M5, M6
M2, M2a, M3
SAR
(b)
Rel. Ab., a.u.
100
80
60
40
20
0
SAR
(c)
Rel. Ab., a.u.
4
2
0
M9
M8
M4
(d)
Rel. Ab., a.u.
20
10
0
M6
M3
(e)
Rel. Ab., a.u.
20
10
0
M11b
M10
M2
(f)
Rel. Ab., a.u.
100
50
0
M10a
M5
M2a
(g)
Rel. Ab., a.u.
6
4
2
0
M8a
M7a
(h)
Rel. Ab., a.u.
4
2
0
M10b
(i)
Rel. Ab., a.u.
40
20
0
M11
M9a
0
5
10
Time, min

Figure 7.

REFERENCES

[1] Ackemann, B.; Berna, J. Current applications of liquid chromatography/mass spectrometry in pharmaceutical discovery after a decade of innovation. *Ann. Rev. Anal. Chem.* **2008**, *1*, 357-396.

[2] McEwen, A.; Henson, C. Quantitative whole-body autoradiography: past, present and future. *Bioanal.* **2015,** *7,* 557-568.

[3] Seymour, M. Themed issue on radioisotopic bioanalysis. *Bioanal*. **2015**, *7*, 499-501.

[4] Solon, E. G. Autoradiography techniques and quantification of drug distribution. *Cell Tissue Res.* **2015**, *360*, 87-107.

[5] Solon E. G.; Schweitzer, A.; Stoeckli, M.; Prideaux, B. Autoradiography, MALDI-MS, and SIMS-MS imaging in pharmaceutical discovery and development. *AAPS J.* **2010**, *12*, 11-26.

[6] Masucci, J. A.; Mahan, A.D.; Kwasnoski, J.D.; Caldwell, G. W. A novel method for determination of drug distribution in rat brain tissue sections by LC/MS/MS: functional tissue microanalysis. *Curr. Top. Med. Chem.* **2012**, *12*, 1243-1249.

[7] Hamm, G.; Bonnel, D.; Legouffe, R.; Pamelard, F.; Delbos, J-M.; Bouzom, F.; Stauber, J. Quantitative mass spectrometry imaging of propranolol and olanzapine using tissue extinction calculation as normalization factor. *J Proteomics* **2012**, *75*, 4952-4961.

[8] Porta, T.; Lesur, A.; Varesio, E,; Hopfgartner, G. Quantification in MALDI-MS imaging: what can we learn from MALDI-selected reaction monitoring and what can we expect for imaging? *Anal. Bioanal. Chem.* **2015**, *407*, 2177-2187.

[9] Chumbley, C. W.; Reyzer, M. L.; Allen, J. L.; Marriner, G. A.; Via, L. E.; Barry III, C. E.; Caprioli, R. M. Absolute quantitative MALDI imaging mass spectrometry: A case of rifampicin in liver tissues. *Anal. Chem*. **2016**, *88*, 2392-2398.

[10] Swales, J. G.; Dexter, A.; Hamm, G.; Nilsson, A.; Strittmatter, N.; Michopoulos, F.; Hardy, C.; Morentin-Gutierrez, P.; Mellor, M.; Andren, P. E.; Clench, M. R.; Bunch, J.; Critchlow, S. E.; Goodwin, R. J. A. Quantitation of endogenous metabolites in mouse tumors using mass-spectrometry imaging. *Anal. Chem*. **2018**, *90*, 6051-6058.

[11] Pirman, D. A.; Reich, R. F.; Kiss, A.; Heeren, R. M. A.; Yost, R. A. Quantitative MALDI tandem mass spectrometric imaging of cocaine from brain tissue with a deuterated internal standard. *Anal. Chem*. **2013**, *85*, 1081-1089.

[12] Groseclose, M. R.; Castellino, S. A mimetic tissue model for the quantification of drug distributions by MALDI imaging mass spectrometry. *Anal. Chem*. **2013**, *85*, 10099-10106.

[13] Luo, Z.; He, J.; He, J.; Huang, L.; Song, X.; Li, X.; Abliz, Z. Quantitative analysis of drug distribution by ambient mass spectrometry imaging method with signal extinction normalization strategy and inkjet-printing technology. *Talanta* **2018**, *179*, 230–237.

[14] Taylor, A. J.; Dexter, A.; Bunch, J. Exploring ion suppression in mass spectrometry imaging of a heterogeneous tissue. *Anal. Chem.* **2018**, *90*, 5637−5645.

[15] Lanekoff, I.; Thomas, M.; Carson, J. P.; Smith, J. N.; Timchalk, C.; Laskin, J. Imaging nicotine in rat brain tissue by use of nanospray desorption electrospray ionization mass spectrometry. *Anal. Chem*. **2013**, *85*, 882−889.

[16] Laskin, J.; Lanekoff, I. Ambient mass spectrometry imaging using direct liquid extraction techniques. *Anal. Chem.* **2016**, *88*, 52−73.

[17] Swales, J. G.; Strittmatter, N.; Tucker, J. W.; Clench, M. R.; Webborn, P. J. H.; Goodwin, R.

J. A. Spatial quantitation of drugs in tissues using liquid extraction surface analysis mass spectrometry imaging. *Sci. Rep.* **2016**, *6*, 37648.

[18] Havlikova, J.; Randall, E. C.; Griffiths, R. L, Swales, J. G.; Goodwin, R. J. A.; Bunch, J.; Styles, I. B.; Cooper, H. J. Quantitative imaging of proteins in tissue by stable isotope labeled mimetic liquid extraction surface analysis mass spectrometry. *Anal. Chem.* **2019**, *91*, 14198-14202.

[19] Wu, Q.; Huang, Z.; Wang, Y.; Zhang, Z.; Lu, H. Absolute quantitative imaging of sphingolipids in brain tissue by exhaustive liquid microjunction surface sampling–liquid chromatography–mass spectrometry. *J. Chrom. A.* **2019**, *1609*, 460436.

[20] Kertesz, V.; Weiskittel, T. M.; Vavrek, M.; Freddo, C.; Van Berkel, G. J. Extraction efficiency and implications for absolute quantitation of propranolol in mouse brain, liver and kidney tissue sections using droplet-based liquid microjunction surface sampling high-performance liquid chromatography/electrospray ionization tandem mass spectrometry. *Rapid Commun. Mass Spectrom.* **2016**, *30*, 1705-1712.

[21] d'Argy, R. Tissue pieces from whole-body sections used for chromatographic separation of metabolites. *Acta Pharmacol. Toxicol. Suppl.* **1977**, *1(41)*, 16–17.

[22] d'Argy, R.; Sundwall. A. Quantitative whole-body radioluminography-Future strategy for balance and tissue distribution studies. *Reg. Toxicol. Pharmacol.* **2000**, *31*, S57–S62.

[23] Koshel, B.; Birdsall, R.; Chen W. Two-dimensional liquid chromatography coupled to mass spectrometry for impurity analysis of dye-conjugated oligonucleotides. *J. Chrom. B.* **2020**, *1137*, 121906.

[24] Chen, Y.; Li, J.; Schmitz, O. J. Development of an At-Column Dilution Modulator for Flexible and Precise Control of Dilution Factors to Overcome Mobile Phase Incompatibility

in Comprehensive Two-Dimensional Liquid Chromatography. *Anal. Chem.* **2019**, *91*, 10251−10257.

[25] Chen, Y.; Montero, L.; Luo, J.; Li, J.; Schmitz O. J. Application of the new at-column dilution (ACD) modulator for the two-dimensional RP×HILIC analysis of Buddleja davidii. *Anal. and Bioanal. Chem.* **2020** *412*,1483–1495.

[26] Stoll, D. R.; Shoykhet, K.; Petersson, P.; and Buckenmaier S. Active Solvent Modulation: A Valve-Based Approach To Improve Separation Compatibility in Two-Dimensional Liquid Chromatography. *Anal. Chem.* **2017**, *89*, 9260−9267.

[27] Pirok, B. W. J.; Gargano, A. F. G.; Schoenmakers, P. J. Optimizing separations in online comprehensive two-dimensional liquid chromatography. *J. Sep. Sci.* **2018**, *41*, 68–98.

[28] Lv, W.; Shi, X.; Wang, S.; Xu, G. Multidimensional liquid chromatography-mass spectrometry for metabolomic and lipidomic analyses. *Trends in Anal. Chem.* **2019**, *120*, 1153024.

[29] Koppen, V.; Looveren, C. V.; Francois, I.; Cuyckens, F. Selective drug metabolite trace analysis by very high-volume injections and heartcut two-dimensional (2D)-ultrahigh performance liquid chromatography (UHPLC) *J. Chrom. A.* **2019**, *1601*, 164–170.

[30] Koppen, V.; Jones, R.; Bockx, M.; Cuyckens, F. High volume injections of biological samples for sensitive metabolite profiling and quantitation *J. Chrom. A.* **2014**, *1372*, 102–109.

[31] Stoll, D. R.; Carr, P. W. Two-Dimensional Liquid Chromatography: A State of the Art Tutorial *Anal. Chem.* **2017**, *89*, 519−531.

[32] Stoll, D. R.; Harmes, D. C.; Danforth, J.; Wagner, E.; Guillarme, D.; Fekete, Sz.; Beck. A. Direct Identification of Rituximab Main Isoforms and Subunit Analysis by Online Selective Comprehensive Two-Dimensional Liquid Chromatography−Mass Spectrometry *Anal. Chem.*

2015, *87*, 8307−8315.

[33] Talus, E. S.; Witt, Klaus E.; Stoll, D. R. Effect of pressure pulses at the interface valve on the stability ofsecond dimension columns in online comprehensivetwo-dimensional liquid chromatography *J. Chrom. A.* **2015**, *1378*, 50–57.

[34] Rowland, M.; Tozer, T. N. Clinical Pharmacokinetics, Concepts and Applications, 3rd edition, **1995**, ISBN 0-683-07404-0